$n + {}^{209}$Bi mean field between -20 and 60 MeV

R. K. Das* and R. W. Finlay
Ohio University, Athens, Ohio 45701
(Received 8 December 1989)

New measurements of differential elastic neutron scattering for ^{209}Bi at energies between 7.5 and 24.0 MeV are presented along with new measurements of σ_T up to 60 MeV. These data, taken together with earlier measurements at lower energy, provide a very large data set for testing and extending the dispersive optical-model analysis. The dispersion correction to the optical model has been obtained from the scattering and total cross-section data. The potential is extrapolated to negative energy for comparison with bound-state properties. A very good description of all of the data is obtained from -20 to $+60$ MeV. The present analysis suggests somewhat less depletion of the Fermi sea in this mass region than has been obtained from electron-scattering data and from other recent treatments of the dispersion correction to the optical model.

I. INTRODUCTION

The nucleon-nucleus optical-model (OMP) at low energy has enjoyed a considerable resurgence in interest over the last few years. Early reports[1,2] that the geometrical parameters of the model showed a distinct dependence on projectile energy were taken[3] as evidence of the dispersion correction[4] to the optical potential. Much of the recent attention has focused on ^{208}Pb in part because of its very special shell-model properties, but also because of the availability of high-quality neutron scattering data.[1,5]

The doubly magic shell structure of ^{208}Pb is a source of difficulty at low projectile energy. Level densities in the target nucleus are low so compound elastic cross sections are larger and fluctuate more rapidly with incident energy than would be expected for nuclei removed from the closed shells. Improper treatment of these fluctuations could lead to errors in the extraction of the shape-elastic-scattering cross sections that could strongly influence the determination of optical-model parameters. The dispersion correction involves an extrapolation of the energy dependence of the empirical imaginary potential from the lowest measured energy to the Fermi energy. Mahaux and Sartor[6] have described the hazards of an extrapolation over a wide range of energies for the $p + {}^{208}$Pb system, and Finlay *et al.*[7] have shown how an improper determination of the optical-model parameters can lead to unreasonable estimates of the dispersion correction.

Lawson, Guenther, and Smith[8] (hereafter LGS) have pointed out the advantages of ^{209}Bi for such a study: ^{209}Bi is monoisotopic and has a large density of states near the neutron binding energy. It offers the prospect of studying shape elastic scattering down to low energies with much less uncertainty from the fluctuations in the compound elastic cross sections. The fact that the compound nucleus cross sections are indeed smaller for ^{209}Bi than for ^{208}Pb was shown by Annand *et al.*[5] in a comparative study of these nuclei in the region $4 < E_n < 7$ MeV.

LGS[8] repeated and extended the study of $n + {}^{209}$Bi of Annand *et al.*[5] with their own new measurements of elastic scattering from 4.5 to 10.0 MeV to which they added earlier data between 1.5 and 4.0 MeV from Argonne[9] and from Studsvik[10] in order to search over a wide energy range for a surface-peaked term in the real part of the optical potential as predicted by the dispersion relation (see Sec. III). Above 10 MeV, LGS connected their empirical results for ^{209}Bi with global optical parameters[11] or with scattering measurements from ^{208}Pb at higher energy.[1] One purpose of the present work was to extend the data base for $n + {}^{209}$Bi scattering to higher energy and to perform a similar analysis in terms of the dispersion correction to the optical potential without recourse to global potential parameters.

A second goal of this work was to examine the nuclear mean field at negative energy by invoking the dispersion correction to extrapolate the optical-model results into the shell-model domain. A brief discussion of the dispersion correction is given in a subsequent section.

II. EXPERIMENTAL METHODS

Differential elastic-scattering cross sections were measured at the Ohio University beam swinger facility for neutron energies of 7.5, 8, 9, 10, 12, 20, and 24 MeV. Experimental procedures have been described many times (see, for example, Refs. 1 and 5). Time-of-flight resolution was adequate to insure that the elastic-scattering peaks were well separated from any inelastically scattered neutron groups. Raw time-of-flight data were corrected for multiple scattering, finite angular resolution, and attenuation of the incident neutron beam using well-established techniques. Errors due to counting statistics were generally less than 3% for scattering angles less than 90 and 3–5 % at larger scattering angles for all of the data between 7.5 and 12 MeV. At 20 and 24 MeV the errors were typically 50% larger than at lower energy and a few points at the back-angle minima had counting errors of over 10%. Data are available in tabular form from the authors and will be forwarded to the National

Nuclear Data Center (Brookhaven, NY) after publication.

None of the new data required correction for compound elastic scattering. Below 7 MeV, compound elastic scattering is important and the detailed corrections that were required are described by Annand *et al.*[3] Some of the new data were reported earlier as part of a conference proceeding.[16]

Total cross sections were measured at the Oak Ridge Electron Linear Accelerator (ORELA) facility of the Oak Ridge National Laboratory. Bremsstrahlung photons are converted into neutrons in a thick beryllium block producing a continuous or "white" neutron spectrum that extends up to 60 MeV. Transmission of the Bi sample was compared to the no-sample or open beam condition with a time-of-flight detector located 80 m from the neutron production target. Errors due to counting statistics were typically less than 0.5% and systematic errors are estimated to be less than 2%. Details of the ORELA group measurements of total cross section are given by Larson *et al.*[17]

III. THE DISPERSION INTEGRAL

Mahaux and Sartor[12] have developed a general representation of the dispersion correction to the phenomenological optical potential that includes both polarization and correlation effects, i.e., that accounts for the finite probability, that the target nucleus does not remain in its ground state during the elastic-scattering process. In this approach, the real part of the mean field $V(r,E)$ is written as the sum of a smoothly varying Hartree-Fock term and a dispersion contribution, i.e.,

$$V(r,E)=V_H(r,E)+\Delta V(r,E) \tag{1}$$

with

$$\Delta V(r,E)=\frac{P}{\pi}\int_{-\infty}^{\infty}\frac{W(r,E')}{E'-E}dE' , \tag{2}$$

where P indicates a principal value and $W(r,E')$ is the imaginary part of the nuclear mean field.

$V_H(r,E)$ is the local equivalent of the energy-independent nonlocal Hartree-Fock field which might be approximated in terms of an energy-dependent depth and an energy-independent Woods-Saxon radial shape, i.e.,

$$V_H(r,E)=V_H(E)f(r_H,a_H) .$$

Over a limited energy range, it should be possible to represent $V_H(E)$ as

$$V_H(E)=V_H(0)e^{-\alpha E} \tag{3}$$

with $\alpha=(m/2\hbar^2)\beta^2$, where β is the range of the nonlocality.

Evaluation of $\Delta V(r,E)$ for nuclear scattering requires knowledge of $W(r,E')$ over the entire energy range from $-\infty$ to ∞. In practice, phenomenological analysis of neutron scattering data provides information about $W(r,E')$ over the very limited positive-energy range from a few MeV to several hundred MeV. The current approach to this problem is to require that (i) the mean field be real at the Fermi energy (E_F), i.e.,

$$W(r,E_F)=0 ,$$

and

$$\Delta V(r,E_F)=0 ,$$

and (ii) the imaginary potential be symmetric about the Fermi energy:

$$W(r,E+E_F)=W(r,E_F-E) .$$

The Fermi energy is taken as the midpoint between the first unoccupied single-particle level and the last occupied single-particle level. For ^{209}Bi, E_F is approximately -6 MeV. The assumption that $W(r,E)$ is symmetric about E_F has been questioned by Delaroche *et al.*,[13] but in the absence of a clear alternative we retain it in the present work.

One further complication in the evaluation of the dispersion integral [Eq. (2)] that must be dealt with in detail is the variation of the radial shape of $W(r,E')$ with energy. It is well known that at low enough energy the absorption is confined to the nuclear surface while at high energy the absorption spreads throughout the volume. Two detailed and quantitative representations of this behavior have been applied with considerable success to the analysis of dispersion corrections for the $n+^{208}$Pb mean field.

(1) The dispersive optical-model analysis (DOMA) of Johnson, Horen, and Mahaux[14] represents the energy dependence of the imaginary potential as a sum of a volume absorption (Woods-Saxon form) and a surface absorption (derivative Woods-Saxon),

$$W(r,E)=W_V(r,E)+W_S(r,E) . \tag{4}$$

The form factors for each term are independent of energy (constant geometry), but the well depths have explicit energy dependence that are to be deduced from the scattering data. Their final real potential consists of three terms: a volume Woods-Saxon term that varies slowly with energy and is identified with the Hartree-Fock term, a volume Woods-Saxon term derived from a dispersion integral over $W_V(r,E)$, and a surface component with energy dependence also derived from the dispersion integral over the surface imaginary potential $W_S(r,E)$, i.e.,

$$V(r,E)=V_H(r,E)+\Delta V_V(r,E)+\Delta V_S(r,E) , \tag{5}$$

where

$$\Delta V_q(r,E)=\frac{P}{\pi}\int_{-\infty}^{\infty}\frac{W_q(r,E')}{E'-E}dE' .$$

It is clear that the interplay of these three terms could result in an energy dependence of the geometrical parameters of a phenomenological potential as discussed in the Introduction.

(2) The iterative moment approach (IMA) of Mahaux and Sartor.[12,15] In this approach, the imaginary potential is represented in terms of the energy dependences of a series of radial moments. The dispersion integral is calculated for each of these moments, and the energy-dependent real central potential is reconstructed from these moments.

The present analysis (Sec. V) is an application of the DOMA approach of Ref. 14 with certain modifications. The data are being reanalyzed in terms of the IMA, but that analysis will be the subject of a separate paper.

IV. PHENOMENOLOGICAL ANALYSIS

In this section we describe three different approaches to the determination of suitable empirical optical model for the $n+^{209}$Bi system. The three approaches are conveniently named as (1) individual best fit, (2) Fourier-Bessel (FB) expansions, and (3) grid searches.

The data base for the present analysis consists of the following measurements: Recent measurements of differential elastic-scattering cross sections at $E_n=7.5$, 8, 9, 10, 11, 12, 20, and 24 MeV at Ohio University together with older measurements at $E_n=4$, 4.5, 5, 5.5, 6, 6.5, and 7 MeV[5] comprises the Ohio University data. Cross-section data at $E_n=1.47$, 1.96, 2.45, 2.96, 3.36 (Ref. 10), and 21.6 MeV (Ref. 18) and $E_n=1.5$, 1.9, 2.5, 3.0, and 3.5 MeV (Ref. 9), as well as new measurements of total cross sections at Oak Ridge National Laboratory from 1.0 to 60.0 MeV were also used in the analysis. While performing the least-squares fit to these 26 different elastic-scattering angular distributions for the three different approaches, total cross sections at each energy were used with an artificially small uncertainty of ±0.1% to give them non-negligible weight compared with the many points in the scattering distributions.

A. Individual best fits

The empirical optical potential is defined as

$$V_R f(r,R_R,a_R)+iW_V f(r,R_I,a_I)-i4W_S a_S \frac{d}{dr} f(r,R_I,a_I)+\mathbf{L}\cdot\sigma\left[\frac{\hbar}{m_\pi c}\right]^2 V_{SO}\frac{1}{r}\frac{d}{dr}f(r,R_{SO},a_{SO}) , \tag{6}$$

where $R_x=r_x A^{1/3}$ and $f(r,R_x,a_x)$ is the radial form factor which is assumed to be a Woods-Saxon (WS) type.

Since there are few measurements of analyzing power data for $n+^{209}$Bi, we assume the spin-orbit (SO) potential to be that for $n+^{208}$Pb,[5] namely

$$V_{SO}=5.75 \text{ MeV}, \quad r_{SO}=1.150 \text{ fm}, \quad a_{SO}=0.499 \text{ fm} .$$

Several different values of the spin-orbit parameters were tried, and, within reasonable limits, no change in the overall quality of the fit to the data was obtained. The main results for the central real and imaginary potentials are not very sensitive to the choice of the spin-orbit potential.

The computer code GENOA (Ref. 19) was used to obtain best fits to the data at each energy by varying the well depths and also the geometrical parameters of the WS form factors. The parameter W_V was included for neutron energies above 10 MeV below which its contribution was negligible.

Best-fit neutron optical-model parameters are given in Table I. Normally one expects to find some scatter in the values obtained from individual best fits, and this is true to some extent here. However, the minimum χ^2 is fairly deep and unambiguous as long as the data set is sufficiently complete and accurate. The result of this search shows that the most rapid variations of these parameters occur in the region $E_n<7$ MeV, while at higher energies the variations are more or less smooth. The volume part of the imaginary potential appears at 12.0 MeV and gradually increases with energy while the surface part starts decreasing.

There are two familiar shortcomings to the individual best-fit analysis. First, it is possible, as can be seen from Table I, that the best fit to the data can be obtained when one or more of the parameters takes on an unreasonable value. Examples of these are the 1.47- and 5-MeV data. The a_I for both these data sets are very low compared to the others. To compensate these low values of the a_I's, the W_D's are much higher. In all the cases, except for the 1.47 and 1.5 MeV, the r_R's are lower than the r_I's as expected. Second, because of the complexity of the multidimensional χ^2 space, it is difficult to assign an uncertainty to the final parameters.

B. The Fourier-Bessel expansion of the central potential

Even though the results of the previous section indicate that the parameters of the Woods-Saxon potential can be well determined from accurate data, it is still possible that this parametrization obscures some of the interesting features of the nucleon-nucleus potential. It is highly desirable to extract the features of the potential well directly from the data without constraining the analysis to the conventional Woods-Saxon form. The Fourier-Bessel expansion method consists of adding a Fourier-Bessel series to the conventional Woods-Saxon central potential and is given by

$$V(r,E)=V(E)f(r)+\sum_{n=1}^{N} a_n j_0(q_n r) , \tag{7}$$

where $q_n=(n\pi/R)$, R being the cutoff radius, and

$$W(r,E)=W_V(E)f(r)-4W_S a_I\frac{df(r)}{dr}+\sum_{n=1}^{N} b_n j_0(q_n r) . \tag{8}$$

The best-fit values of V_R, W_V, W_S, r_R, a_R, r_I, and a_I are inserted into Eqs. (7) and (8) and held fixed for the FB fit. Then a search for the parameters a_n and b_n is performed. The number of coefficients needed for the real and imaginary parts of the series is determined by the minimization of χ^2 per degree of freedom, and the values

TABLE I. Best-fit neutron optical-model parameters for ^{209}Bi. The spin-orbit potential was fixed at $V_{SO}=5.75$ MeV, $r_{SO}=1.105$ fm, and $a_{SO}=0.499$ fm.

E_n (MeV)	V_R (MeV)	r_R (fm)	a_R (fm)	W_V (MeV)	W_D (MeV)	r_I (fm)	a_I (fm)	χ^2/N
1.475	43.154	1.308	0.568	0.0	14.018	1.296	0.174	0.46
1.50	46.122	1.246	0.605	0.0	8.770	1.177	0.280	0.11
1.90	46.061	1.242	0.507	0.0	4.108	1.251	0.487	0.42
1.962	46.749	1.216	0.752	0.0	5.591	1.248	0.367	0.59
2.451	46.453	1.215	0.793	0.0	6.236	1.250	0.440	0.60
2.50	45.278	1.242	0.726	0.0	6.554	1.275	0.363	0.17
2.961	46.548	1.211	0.818	0.0	4.744	1.333	0.424	7.57
3.00	44.321	1.246	0.764	0.0	6.550	1.346	0.335	0.16
3.358	49.756	1.158	0.832	0.0	4.370	1.344	0.512	0.87
3.53	45.235	1.244	0.722	0.0	7.061	1.324	0.315	0.51
4.00	43.810	1.293	0.622	0.0	8.066	1.308	0.319	1.70
4.50	44.953	1.258	0.733	0.0	8.999	1.345	0.285	4.35
5.00	43.242	1.288	0.760	0.0	15.819	1.360	0.167	3.42
5.50	41.935	1.303	0.762	0.0	9.441	1.391	0.328	3.88
6.00	43.607	1.280	0.701	0.0	10.788	1.352	0.273	7.52
6.50	44.042	1.267	0.675	0.0	8.431	1.332	0.333	13.32
7.00	43.767	1.256	0.671	0.0	4.360	1.307	0.671	46.41
7.50	46.960	1.212	0.646	0.0	5.340	1.309	0.560	30.67
8.00	41.228	1.251	0.727	0.0	8.624	1.323	0.352	71.83
9.00	46.150	1.207	0.728	0.0	5.630	1.299	0.582	14.68
10.00	46.050	1.209	0.725	0.0	6.040	1.281	0.589	21.84
11.00	43.515	1.254	0.657	0.0	7.556	1.268	0.519	14.08
12.00	43.968	1.246	0.672	0.043	7.841	1.249	0.515	8.36
20.00	41.446	1.250	0.669	1.436	8.002	1.251	0.435	15.09
21.60	42.645	1.227	0.683	1.584	6.272	1.239	0.524	25.68
24.00	43.607	1.196	0.628	3.367	2.257	1.320	0.705	35.25

of the coefficients are determined by a least-squares fit to the data. The number of terms used in the Fourier-Bessel expansion was found to depend weakly on energy, and good convergence was obtained at a large cutoff radius (12 fm, independent of energy). The final results for both the real and imaginary potentials were not sensitive to the choice of the initial Woods-Saxon potential, but the calculations are faster when best-fit values are used.

By introducing a matrix inversion routine into GENOA, the covariance matrix M of the parameters a_n may be obtained from the secular equations that minimize χ^2/N. The diagonal elements of M are the errors in the coefficients a_n and the off-diagonal elements contain the correlations among them. With these quantities, one can construct a much better statement of the uncertainties in certain quantities of interest (i.e., real and imaginary volume integrals, rms radii) than is possible with the individual best fits of Sec. IV A.

The values of the real (J_V/A) and imaginary (J_I/A) volume integrals per nucleon and the rms radii, together with their uncertainties, are given in Table II. Fits to the differential cross-section data (not shown) obtained using the Fourier-Bessel expansion are uniformly and frequently significantly better than those with the standard Woods-Saxon form factor as indicated by a comparison of χ^2 per data point in Tables I and II.

C. Grid searches

1. Search for the geometrical parameters of the fixed geometry model

In order to carry out a dispersion analysis of the data in the spirit of the DOMA,[14] it is necessary to replace the fluctuating results of Secs. IV A and B with some approximate model for the geometrical parameters of the potential. This is accomplished by means of a grid search discussed briefly below. The eventual dispersion analysis is much more convenient, however, if certain constraints are placed on some geometrical parameters at the outset. Following Johnson, Horen, and Mahaux,[14] we require (1) that the geometrical parameters be independent of energy, (2) that the two terms in the imaginary potential, W_V and W_S, may have differing geometries, i.e., $f(r,R_V,a_V)$ and $f(r,R_S,a_S)$, respectively, and (3) that the geometry of the volume imaginary term be identical with that of the real central Hartree term, i.e.,

$$r_H=r_V$$

and

$$a_H=a_V\ .$$

Determination of geometrical parameters was done

TABLE II. Fourier-Bessel analysis with best-fit neutron optical potentials for ^{209}Bi. Note that the calculations minimized the χ^2 per degree of freedom while the quantity tabulated is the χ^2 per data point. The spin-orbit was fixed at $V_{SO}=5.75$ MeV, $r_{SO}=1.105$ fm, and $a_{SO}=0.499$ fm.

E_N (MeV)	No. of real coeffs.	No. of imaginary coeffs.	$J_V/A\pm\Delta J$ (MeV fm^3)	$R_{rms}\pm\Delta R$ (fm)	$J_I/A\pm\Delta J$ (MeV fm^3)	χ^2/N
1.475	2	2	426.72±6.46	6.37±0.14	34.44±4.50	0.46
1.50	2	4	397.77±2.23	6.16±0.04	24.85±6.55	0.14
1.90	3	3	391.66±4.70	5.99±0.09	15.42±6.62	0.34
1.962	2	2	390.17±4.90	6.25±0.12	26.82±4.27	0.34
2.451	2	2	388.50±5.90	6.30±0.14	38.36±5.26	0.37
2.50	3	2	396.02±12.99	6.37±0.24	34.90±4.17	0.17
2.961	2	2	387.72±5.49	6.32±0.13	34.47±5.25	0.67
3.00	3	3	382.23±16.01	6.34±0.36	42.52±8.41	0.16
3.358	2	2	369.07±4.76	6.13±0.12	34.51±5.30	0.72
3.530	2	3	402.61±2.92	6.35±0.06	35.25±4.25	0.11
4.00	3	2	427.46±9.35	6.31±0.19	35.67±3.65	1.24
4.50	5	2	420.95±22.94	6.52±0.51	38.53±4.04	2.79
5.00	5	2	432.82±11.59	6.66±0.23	39.30±4.90	2.28
5.50	4	3	425.89±7.91	6.67±0.16	56.87±4.87	2.38
6.00	6	2	429.63±15.40	6.49±0.32	45.21±2.29	4.26
6.50	7	2	415.18±19.96	6.40±0.44	41.62±1.60	7.88
7.00	5	5	391.79±5.86	6.30±0.13	52.95±5.92	6.35
7.50	5	4	394.84±5.01	6.24±0.11	49.56±2.96	11.91
8.00	7	2	394.37±8.68	6.42±0.19	54.61±1.38	7.09
9.00	5	5	372.32±5.14	6.19±0.12	54.20±3.97	7.20
10.00	5	5	373.80±5.29	6.21±0.12	52.38±3.51	14.73
11.00	7	6	390.35±8.40	6.27±0.18	59.89±4.95	2.97
12.00	9	4	389.37±9.97	6.26±0.23	59.69±1.34	1.82
20.00	2	3	367.24±3.81	6.23±0.09	59.87±1.99	10.28
21.60	5	4	359.49±6.75	6.24±0.14	57.80±2.57	4.41
24.00	7	3	330.06±4.71	6.06±0.12	61.63±1.94	3.60

with the computer code OPSTAT.[20] Keeping the geometrical parameters fixed at a certain value, a search for the real volume potential and the imaginary volume and surface potential was done. First the volume radius was fixed at a value of 1.1 fm with the other geometrical parameters kept at values of Ref. 5. The potential depths were searched keeping a close watch on the χ^2 per point at each energy. Then the value of r_V was increased at a step size of 0.1 fm. When the χ^2 per point of all the data points hit a minimum value between two values of r_V (e.g., r_V had a minimum χ^2/N between 1.2 and 1.3), a step size of 0.01 fm was used. The process was repeated to get an accuracy to the third decimal place. Now this value of r_V was kept fixed and a similar process was repeated for a_V, r_S, and a_S.

The grid search yielded the following values for the parameters of this constant geometry model:

$$r_H=r_V=1.237 \text{ fm},$$

$$a_H=a_V=0.685 \text{ fm},$$

$$r_S=1.261 \text{ fm}, \quad a_S=0.569 \text{ fm}.$$

2. *Energy dependence of the imaginary potential terms*

Once the geometrical parameters are found, they are kept fixed for this model in order to study the energy dependence of the well depths. With these geometries, a search of four parameters (W_V, W_S, ΔV_S, and V_V) was done at 26 different energies. However, V_V represents the real volume component of the mean field and in this model it corresponds to the sum of V_H and ΔV_V. The best-fit values of W_S and W_V are represented by points in Figs. 1 and 2.

In order to perform the dispersion integral in Eq. (2), it is necessary to represent the variation of potential depths $W_V(E)$ and $W_S(E)$ in suitable functional forms. Trials with linear segment parametrization and other forms were attempted[21] and the best forms are

$$W_S(E)=\frac{c_1(E-E_F)^4 e^{-g|E-E_F|}}{(E-E_F)^4+d^4} \text{ MeV}, \tag{9a}$$

$$W_V(E)=\frac{c_2(E-E_F)^4}{(E-E_F)^4+h^4} \text{ MeV}. \tag{9b}$$

Fitting Eq. (9) to the values of $W_S(E)$ in Fig. 1 yields the solid curve in Fig. 1 with parameter values

$$c_1=12.05 \text{ MeV},$$

$$g=+0.031 \text{ MeV}^{-1},$$

and

$$d=9.8 \text{ MeV}.$$

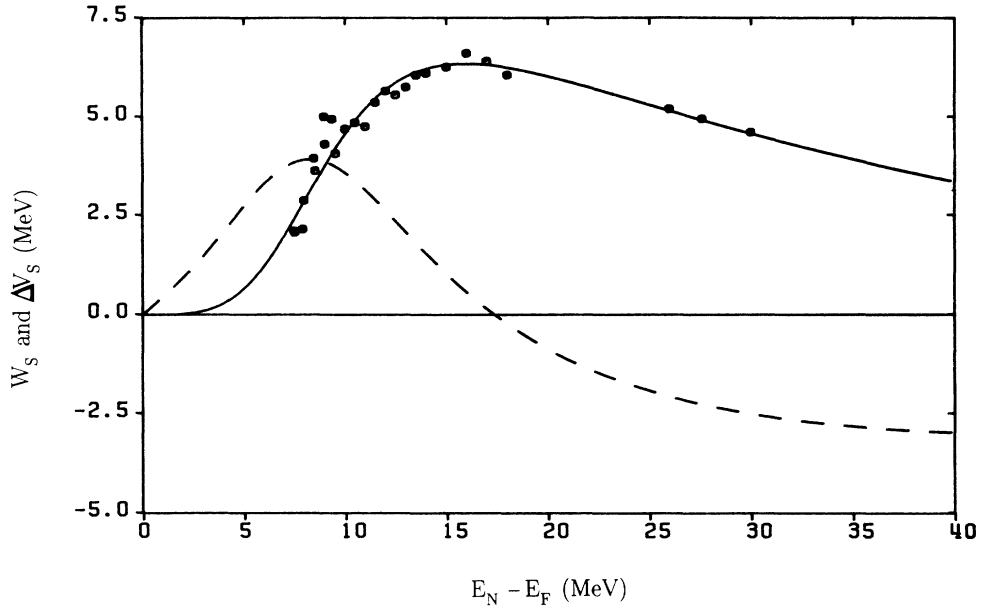

FIG. 1. Depth of the imaginary surface (W_S) as obtained from individual best fits (circles). The solid line represents the absorptive potential obtained from the functional representations defined in Eq. (9a) and the dashed line is the dispersive correction term ΔV_S.

The s- and p-wave strength functions S_0 and S_1, together with the scattering length R' at 70 keV, were examined to provide a guide for $W_S(E)$ at very low energies, but the experimental uncertainties in S_0 and S_1 propagated into 50% uncertainty in W_S, so this constraint was not used in the subsequent analysis.

The volume imaginary potential $W_V(E)$ is not as well known as $W_S(E)$ due to the lack of elastic-scattering data above 24 MeV, but the new measurements of total cross section up to 60 MeV are well described by $W_V \simeq 7$ MeV. Thus, we take

$$c_2 = 7.0 \text{ MeV}$$

and

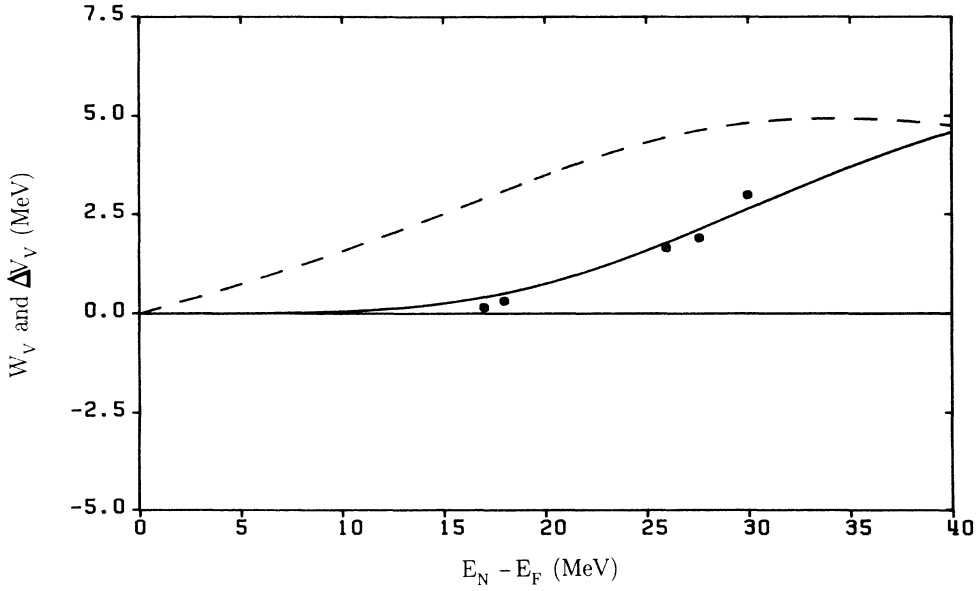

FIG. 2. Depth of imaginary volume (W_V) as obtained from individual best fit (circles). The solid line represents the functional representation defined in Eq. (9b) and the dashed line is the dispersive correction term ΔV_V.

$h=34.5$ MeV

and show this as the solid curve in Fig. 2.

V. THE DISPERSION CORRECTION

In the present work, we performed the dispersion correction for the volume potential analytically with the result

$$\Delta V_V(E)=\frac{c_2 h(E-E_F)[(E-E_F)^2+h^2]}{\sqrt{2}[(E-E_F)^4+h^4]}\ \text{MeV} . \quad (10)$$

The dispersion integral for $\Delta V_S(E)$ was performed numerically. The results are shown as dashed lines for $\Delta V_S(E)$ and $\Delta V_V(E)$ in Figs. 1 and 2, respectively. Numerical values for these energy-dependent well depths are given in Table III. Since there is no further possibility of parameter variation, these values of $\Delta V_S(E)$ and $\Delta V_V(E)$ are straightforward predictions of the dispersion theory. Whether or not they provide a consistent description of the data or an improved understanding of the phenomenological potential will be examined in the present section.

The final results of the fixed geometry grid search were values of W_V, W_S, V_V, and ΔV_S at each of the 26 energies for which differential elastic-scattering data are available. The assumed Hartree-Fock term can be extracted by subtracting the predicted volume dispersion correction from the fitted values for V_V, i.e.,

$$V_H(E)=V_V(E)\Big|_{\text{grid search}}-\Delta V_V(E)\Big|_{\text{predicted}} , \quad (11)$$

since $\Delta V_V(r,E)$ was constructed to have the same geometry as $V_H(r,E)$. Results are shown in Fig. 3 where the small circles come from fits to the scattering data and the large circles are based on fits to the total cross-section data at 30, 36, 45, 50, and 60 MeV. Large plotting symbols are used as a reminder that optical-model parameters obtained from total cross-section data alone are not as well determined as they are from detailed differential scattering cross-section measurements.

The square symbols at negative energy in Fig. 3 are obtained by fitting the binding energy of known single-particle bound states by a procedure discussed at greater length in Sec. VI.

The resulting values for $V_H(E)$ in Fig. 3 are well described by the function specified in Eq. (3), i.e.,

$$V_H(E)=-46.4\exp[-0.34(E-E_F)/46.4] , \quad (12)$$

which is in very good agreement with the results of Johnson *et al.*[14]

$$V_H(E)=-46.4\exp[-0.31(E-E_F)/46.4]$$

for ^{208}Pb. The coefficient $\alpha=0.0073$ MeV^{-1} and the corresponding nonlocality range $\beta=0.78$ fm is not far from the value $\beta=0.85$ fm taken by Perey and Buck[22] in their original work on nonlocal potentials. We conclude that it is possible to find a reasonable representation for $V_H(r,E)$ that meets the expectation of smoothness over a substantial energy range.

A second test of the present application of the DOMA is to compare the predictions for $\Delta V_S(E)$ [obtained by applying the dispersion relation to $W_S(E)$] to the values of $\Delta V_S(E)$ obtained in the grid search. The dashed curve in Fig. 4 is the same as the dashed curve in Fig. 1 but now extended to negative energies. The circles come from fits to the scattering data while the squares come

TABLE III. Energy-dependent well depths for the correction terms ΔV_V and ΔV_S. The geometries for these terms were given in Sec. IV C 1.

E (MeV)	ΔV_V (MeV)	ΔV_S (MeV)	E (MeV)	ΔV_V (MeV)	ΔV_S (MeV)
−20	−2.28	−1.61	22	4.65	−2.32
−18	−1.90	−2.72	24	4.81	−2.52
−16	−1.54	−3.69	26	4.91	−2.67
−14	−1.21	−4.04	28	4.95	−2.80
−12	−0.89	−3.39	30	4.94	−2.89
−10	−0.58	−2.14	32	4.88	−2.96
−8	−0.29	−0.95	34	4.79	−3.02
−6	0	0	36	4.68	3.05
−4	0.29	0.95	38	4.55	−3.08
−2	0.58	2.14	40	4.41	−3.09
0	0.89	3.39	42	4.26	−3.09
2	1.21	4.04	44	4.11	−3.08
4	1.54	3.69	46	3.96	−3.07
6	1.90	2.72	48	3.82	−3.05
8	2.28	1.61	50	3.68	−3.02
10	2.67	0.62	52	3.54	−2.99
12	3.06	−0.19	54	3.41	−2.96
14	3.44	−0.83	56	3.29	−2.93
16	3.81	−1.34	58	3.18	−2.89
18	4.14	−1.74	60	3.07	−2.85
20	4.42	−2.06			

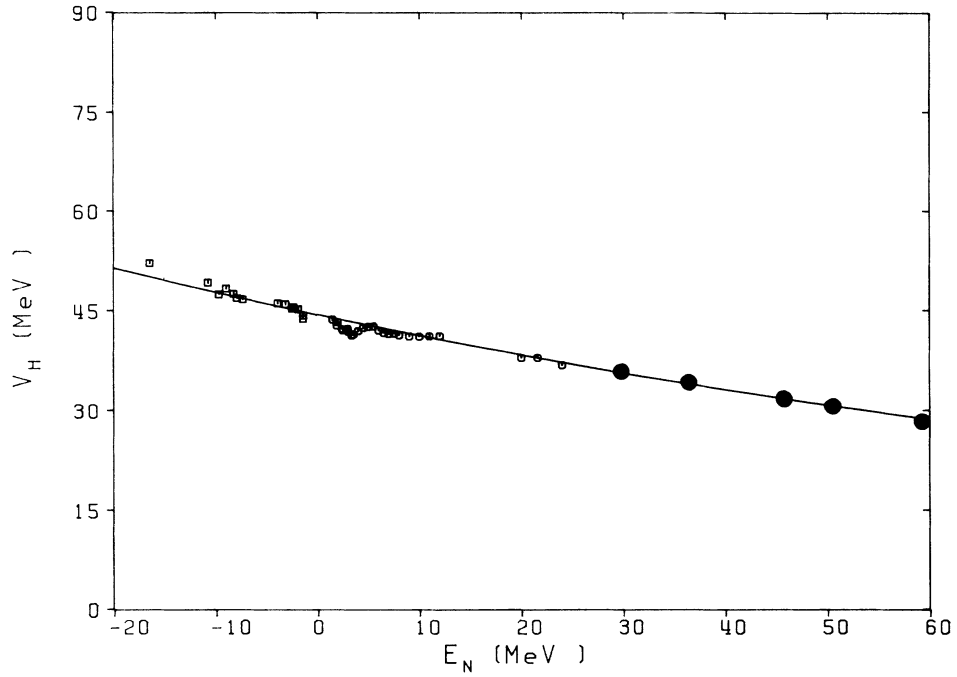

FIG. 3. Energy dependence of the depth of empirical Hartree-Fock potential $V_H(E)$. The open circles represent the individual best fits from differential cross-section data, closed circles from total cross-section data, and squares from the bound states. The line represents the form obtained from Eq. (3).

from the bound states. There appears to be good general agreement between the predicted dispersion relation curve and the empirical points.

A third test of the model comes from comparing predictions of the full dispersion-corrected potential with the full set of scattering observables. This comparison is carried out in Fig. 5 for the 26 sets of differential cross-section measurements. The DOMA gives a very good overall description of the scattering data. The phase of $\sigma(\theta)$ is generally very well reproduced; however, at higher angles, the agreement with the data is not perfect. One plausible explanation for this drawback is the reliance on Woods-Saxon form factors. Indeed, the significant improvement in χ^2/N for the Fourier-Bessel calculations in Sec. IV B over the individual best-fit results generally occurred at large angles.

Finally, the new measured values of the total cross section are shown to be in good agreement with the model in Fig. 6.

In Fig. 7 we show the energy dependence of the volume integral per nucleon

$$\frac{J_V}{A}=\frac{4\pi}{A}\int r^2V(r,E)dr \tag{13}$$

and the root-mean-square radius

$$R_{\rm rms}=\left[\frac{\int r^4V(r,E)dr}{\int r^2V(r,E)dr}\right]^{1/2} \tag{14}$$

for the full potential (solid line) and for the underlying Hartree-Fock-type potential V_H (dashed line). The points at positive energy are derived from the individual best fits to the data (Table I), but they are assigned errors consistent with Fourier-Bessel analysis of the scattering data (Sec. IV B). The points at negative energy are discussed in Sec. VI. It is clear from Fig. 7 that the geometry of the final potential is energy dependent (due to the waxing and waning of ΔV_S) even though all of the geometrical input parameters are constants.

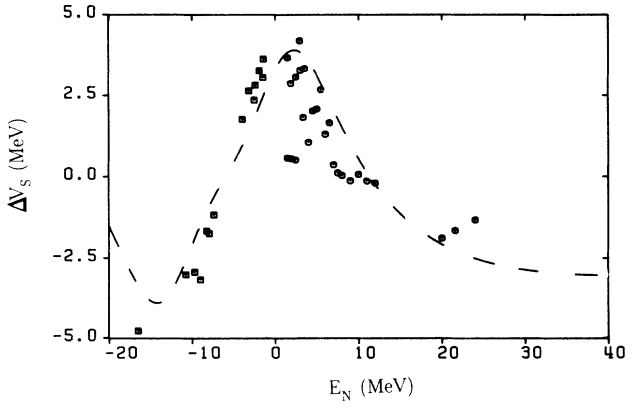

FIG. 4. Depth of the real surface (ΔV_S) as obtained from individual best fit. Open circles are from differential scattering cross-section data and squares from bound states. Dashed line represents the dispersive correction term obtained from W_S.

VI. EXTRAPOLATION TO NEGATIVE ENERGY

The mean field $V(r,E)$ is a continuous function of energy and it varies smoothly but nontrivially when E changes sign. One of the most appealing features of this dispersive optical-model potential is that the shell-model potential for bound states may be obtained by extrapolating the real part of the optical potential toward negative energies. Moreover, this extrapolation is entirely fixed from the dispersion analysis of the scattering data. There are no free parameters in the construction of the shell-model potential. However, in order to test the success of the procedure, one needs to know the properties of the bound states in the $n\pm^{209}$Bi system. Since there is little information concerning the single-particle states in these odd-odd nuclei, we take the attitude that the OMP for ^{209}Bi can be extrapolated to negative energies to describe the bound states in $n\pm^{208}$Pb. This seems to be quite reasonable since the real part of the OMP for ^{209}Bi has been shown[5] to be practically identical to that for ^{208}Pb. [In the global potential model of Rapaport,[23] the two well depths should differ by 132 keV since the values of $(N-Z)/A$ are not quite identical.] The same approach was taken by LGS (Ref. 8) in their study of the optical potential for bismuth. Experimental values for the binding energies of the single-particle states are taken from Refs. 24–26.

At each of the single-particle energies E_{nlj}, the DOMA

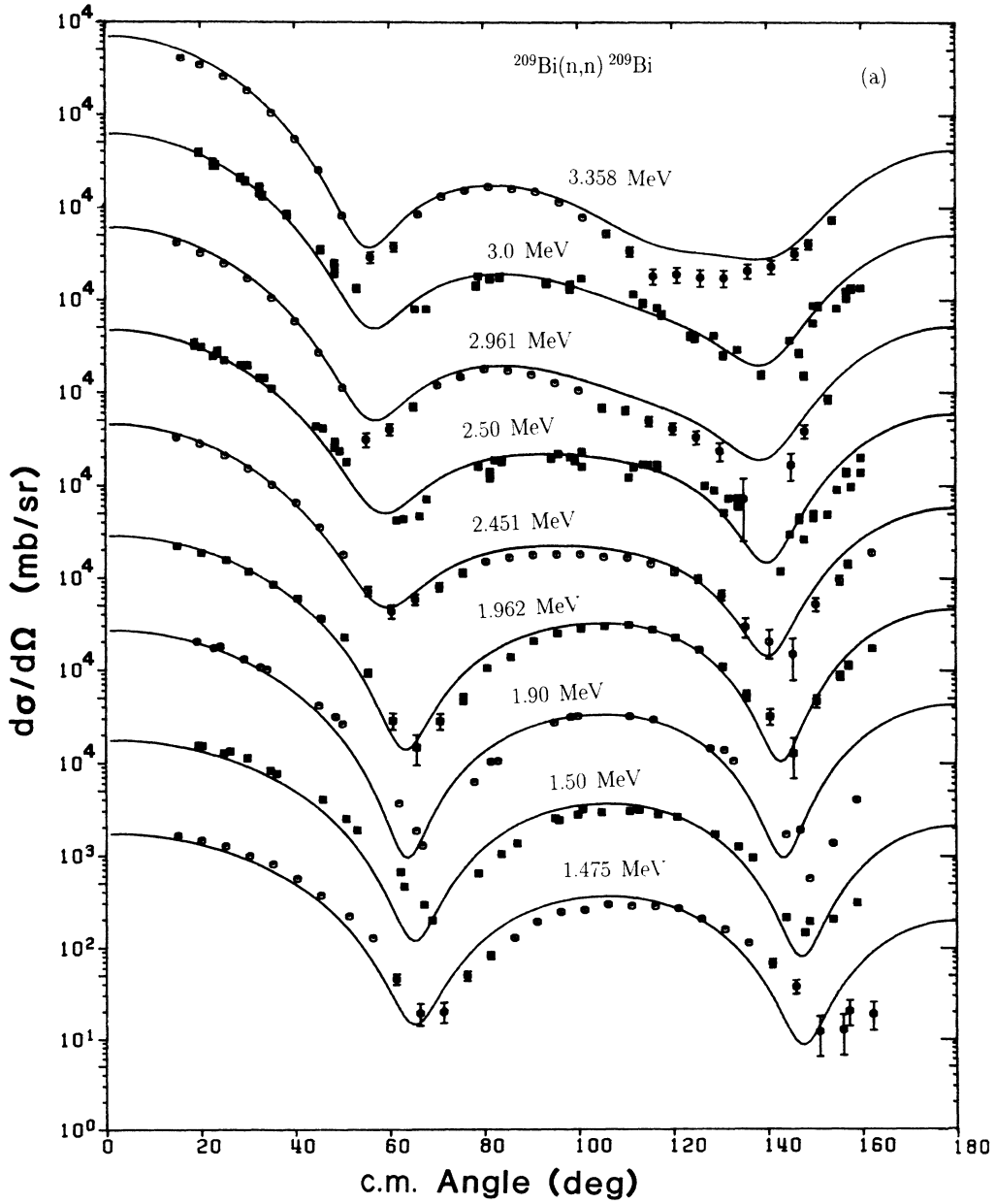

FIG. 5. Comparison between experimental differential scattering cross section and theoretical predictions at different energies. Error bars are displayed whenever they are larger than the plotting symbols.

potential can be searched to provide one number. We perform these calculations twice. First, we assume that

$$V_V(E_{nlj}) = V_H(E_{nlj}) + \Delta V_V(E_{nlj})$$

is given exactly by the DOMA and the surface dispersion term can be searched for the well depth $\Delta V_S(E_{nlj})$ that gives the correct binding energy for that state. This procedure yields the squares in Fig. 4 which are seen to be in excellent agreement with the predicted form of $\Delta V_S(E)$. Alternatively, we can hold $\Delta V_S(E_{nlj})$ to the values given by the DOMA (dashed line in Fig. 4) and search for the optimum value of $V_V(E_{nlj})$. By subtracting the DOMA values for $\Delta V_V(E_{nlj})$ from these optimum values, we obtain $V_H(E_{nlj})$. These values are plotted as the squares in Fig. 3, which, again, are in very good agreement with the model values of $V_H(E)$.

A. Single-particle energies

The effects of the two correction terms ΔV_V and ΔV_S on the spectrum of single-particle energies in ^{208}Pb are shown in Table IV and in Fig. 8. It is clear that the energy spectrum predicted by the smooth term $V_H(E)$ is spread out much more than the experimental spectrum,

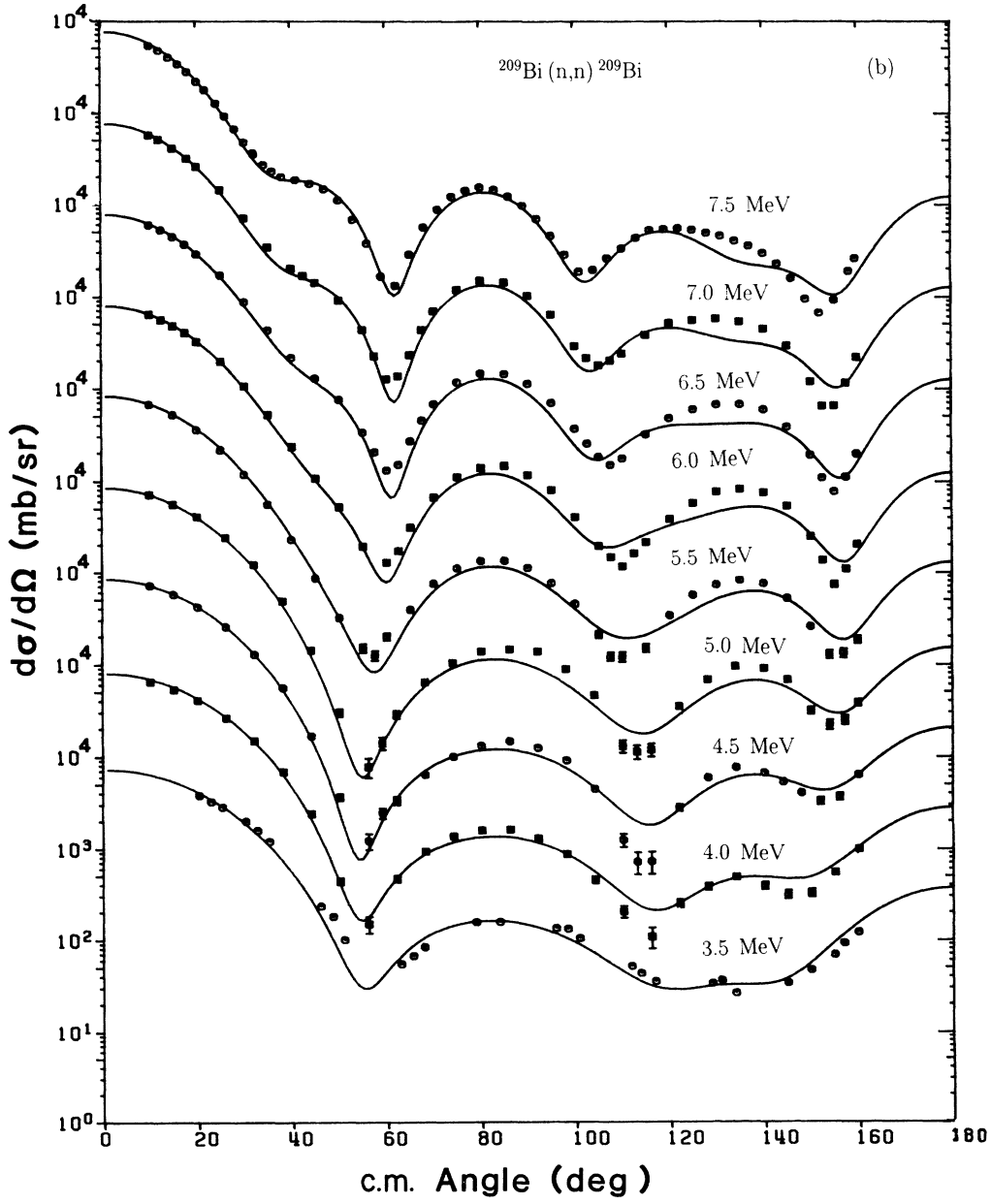

FIG. 5. (*Continued*).

but the inclusion of both correction terms yields a more compressed spectrum that is in much better agreement with the data.

The average energy of a particle (p) or hole (h) valence shell is defined as

$$\langle E_p \rangle = \sum_{\text{uno}} (2j+1)E_{nlj} \Big/ \sum_{\text{uno}} (2j+1) , \quad (15)$$

$$\langle E_h \rangle = \sum_{\text{occ}} (2j+1)E_{nlj} \Big/ \sum_{occ} (2j+1) , \quad (16)$$

where "uno" and "occ" refer to the subshells of the normally unoccupied and occupied valence shells, respectively. The particle-hole gap $\delta_{ph} = \langle E_p \rangle - \langle E_h \rangle$ is reduced from 9.77 MeV in the Hartree-Fock (HF) approximation to 7.01 MeV which is in good agreement with the experimental value $\delta_{ph} = 6.62$ MeV.

B. Other bound-state properties

To complete the analysis, the empirical mean-field potential is used to calculate other properties of bound states.

1. Single-particle wave functions and spectroscopic factors

Normalizing the radial wave functions $\overline{U}_{nlj}(r)$, the spectroscopic factor is given by[27]

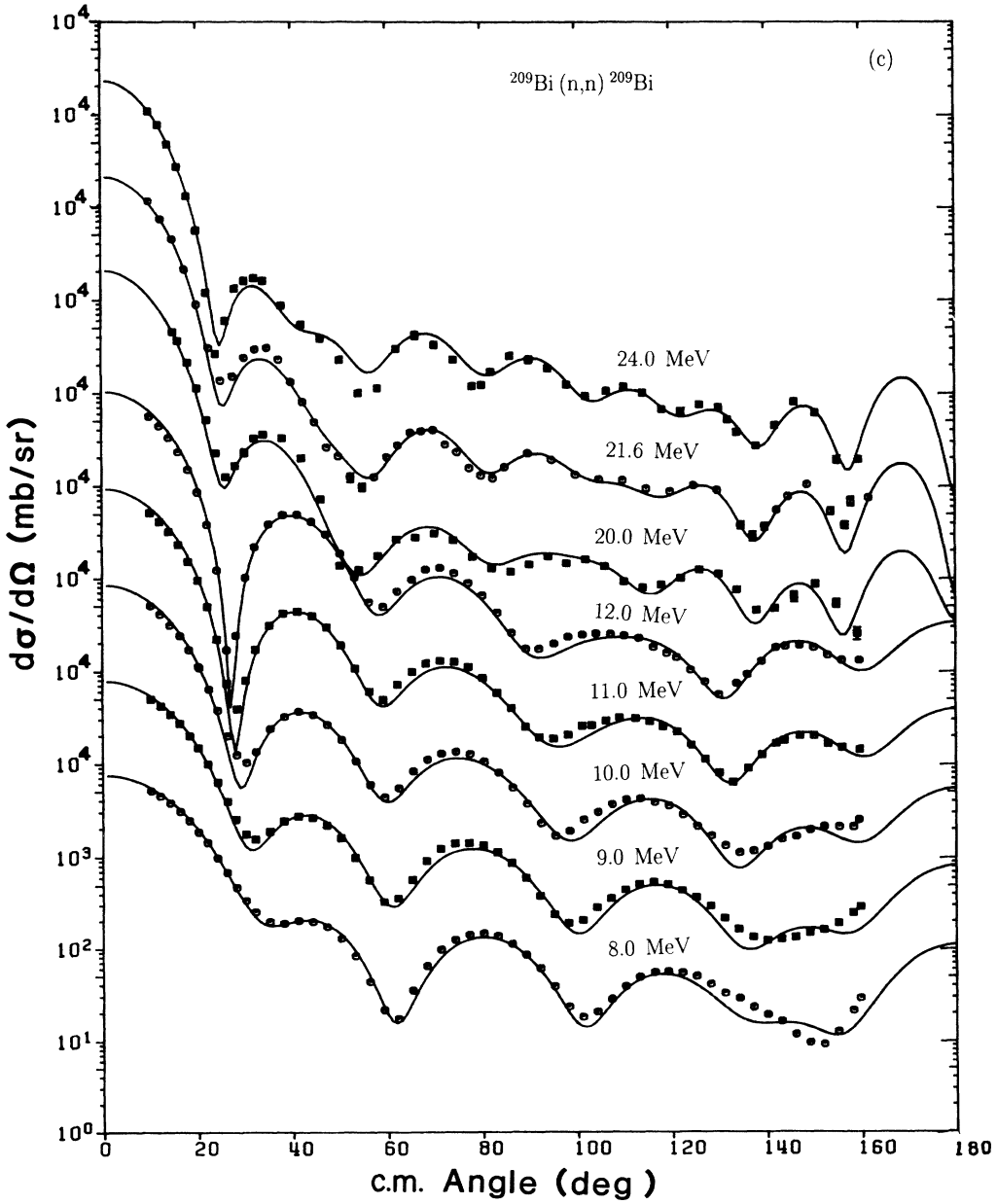

FIG. 5. (*Continued*).

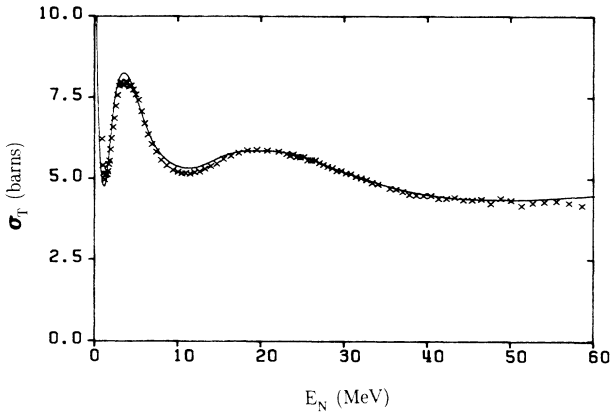

FIG. 6. Neutron total cross-section values σ_T. Model calculations for σ_T are shown by the solid line.

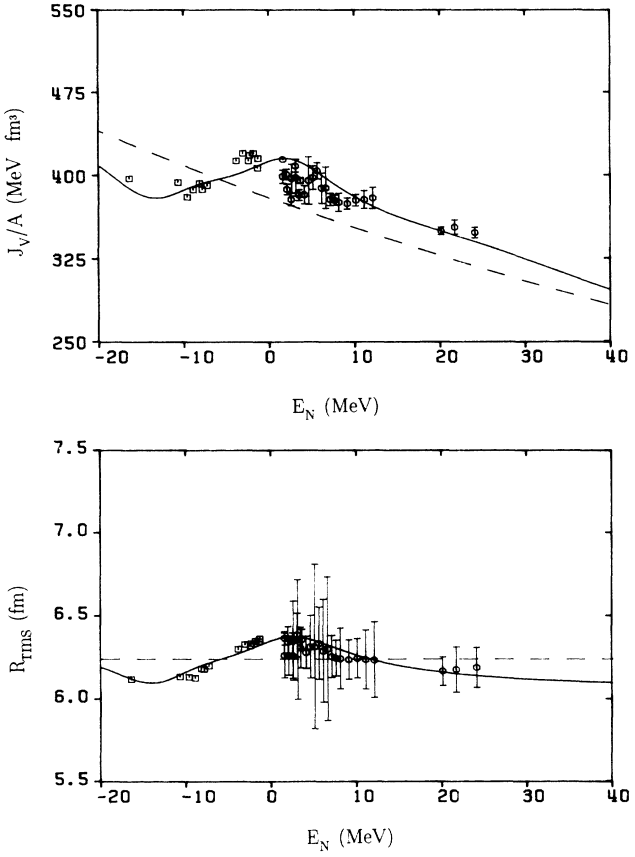

FIG. 7. (Top) Energy dependence of the volume integral of the real part of the full potential. Squares are for bound states. Circles are the individual best-fit values from Table I and the errors are estimates of the uncertainty in this quantity from the Fourier-Bessel analysis of Sec. IV B. The solid line is the prediction from the DOMA analysis and the dashed line is Hartree-Fock contribution. (Bottom) Energy dependence of the root-mean-square radius of the real part of the potential. Plotting symbols have the same meanings as in the top figure.

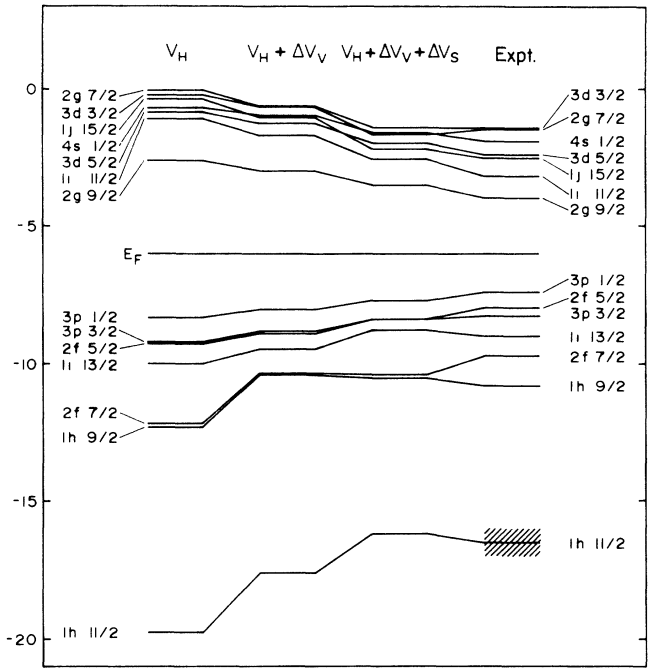

FIG. 8. Neutron single-particle energies E_{nlj} in ^{208}Pb. The first column on the left-hand side gives the calculated values obtained with the Hartree-Fock potential V_H. The second column gives those calculated with the volume dispersion added to V_H while the third column gives the full model potential for the mean field $V_H + \Delta V$. The column labeled EXPT contains the experimental values of ^{208}Pb.

TABLE IV. Neutron single-particle energies E_{nlj} in ^{208}Pb using real potential of $n + ^{209}$Bi. The left-hand column gives the total, orbital angular-momentum, and total angular-momentum quantum numbers, respectively. The column labeled V_H gives the HF values, the column labeled $V_H + \Delta V_V$ gives values with volume dispersion correction added to the HF field, and the column labeled $V_H + \Delta V$ gives the values with the full model potential. The right-hand column gives the experimental values. All energies are in MeV.

nlj	V_H	$V_H+\Delta V_V$	$V_H+\Delta V+\Delta V_S$	Expt.
$3d_{3/2}$	−0.21	−0.58	−1.37	−1.40
$2g_{7/2}$	−0.05	−0.60	−1.66	−1.44
$4s_{1/2}$	−0.68	−0.97	−1.58	−1.90
$3d_{5/2}$	−0.86	−1.25	−1.97	−2.37
$1j_{15/2}$	−0.35	−1.02	−2.18	−2.51
$1i_{11/2}$	−1.07	−1.69	−2.55	−3.16
$2g_{9/2}$	−2.62	−2.99	−3.52	−3.94
$\langle E_p \rangle$	−0.89	−1.43	−2.32	−2.63
$3p_{1/2}$	−8.29	−8.03	−7.69	−7.37
$2f_{5/2}$	−9.26	−8.85	−8.35	−7.94
$3p_{3/2}$	−9.19	−8.80	−8.34	−8.26
$1i_{13/2}$	−9.98	−9.45	−8.78	−9.00
$2f_{7/2}$	−12.19	−11.35	−10.37	−9.71
$1h_{9/2}$	−12.33	−11.39	−10.52	−10.78
$\langle E_h \rangle$	−10.67	−10.03	−9.32	−9.25
$1h_{11/2}$	−19.74	−17.58	−16.17	−16.50

$$S_{nlj}=\int_0^\infty \bar{U}^2_{nlj}(r)[m/\bar{m}(r,E_{nlj})]dr\ , \tag{17}$$

where

$$\frac{\bar{m}(r,E_{nlj})}{m}=1-\frac{d}{dE}\Delta V(r,E)\bigg|_{E=E_{nlj}}\ . \tag{18}$$

2. Occupation probabilities

The occupation probability of the single-particle state (n,l,j) is approximately given for the hole states[27] by

$$N_{nlj}=\int_0^\infty \bar{U}^2_{nlj}(r)\left[1+\frac{1}{\pi}\int_{E_F}^\infty \frac{W(r,E')}{(E'-E_{nlj})^2}dE'\right]dr\ , \quad E_{nlj}<E_F \tag{19}$$

and for particle states by

$$N_{nlj}=-\int_0^\infty \bar{U}^2_{nlj}(r)\left[\frac{1}{\pi}\int_{-\infty}^{E_F} \frac{W(r,E')}{(E'-E_{nlj})^2}dE'\right]dr\ , \quad E_{nlj}>E_F\ . \tag{20}$$

3. The rms radius of valence orbits

The rms radius of each orbit nlj is given by

$$R^{\rm rms}_{nlj}=\left[\int_0^\infty \bar{U}^2_{nlj}r^2dr\right]^{1/2}\ . \tag{21}$$

Table V lists the values of spectroscopic factors, occupation probabilities, and rms radius for each bound state. As discussed before, the real part of the optical potential of $n+^{209}$Bi has been used to calculate these values in ^{208}Pb.

The spectroscopic factors in Table V tend to be lower than those obtained for ^{208}Pb by Johnson *et al.*[14] by an amount ranging from about 0.02 and 0.10. They lie somewhat closer to values recently obtained by Mahaux and Sartor[28] using the variational moment approach (VMA), but that agreement is probably not meaningful since a new prescription for calculating S_{nlj} was given in Ref. 28 which reduces the calculated spectroscopic factors by 0.05–0.1. The differences between the present work and that of Johnson *et al.* are attributed to the slightly different results for $\Delta V(r,E)$ in the integrand for S_{nlj} [see Eqs. (17) and (18)]. These differences in ΔV, in turn, can be traced to the parametric forms chosen for $W_S(E)$ and $W_V(E)$. Reference 14 used simple line segments whereas the present work used the somewhat more realistic forms given by Eq. (9).

TABLE V. Spectroscopic factors, occupation numbers, and rms radii of valence neutron particle and hole states in ^{208}Pb using the real potential of $n+^{209}$Bi.

nlj	S_{nlj}	N_{nlj}	$R^{(\rm rms)}_{nlj}$ (fm)
$3d_{3/2}$	0.814	0.064	7.668
$2g_{7/2}$	0.761	0.085	6.910
$4s_{1/2}$	0.838	0.057	8.125
$3d_{5/2}$	0.804	0.071	7.309
$1j_{15/2}$	0.716	0.107	6.641
$1i_{11/2}$	0.742	0.101	6.415
$2g_{9/2}$	0.779	0.101	6.473
$3p_{1/2}$	0.792	0.893	6.076
$2f_{5/2}$	0.774	0.895	5.980
$1i_{13/2}$	0.757	0.892	6.276
$2f_{7/2}$	0.765	0.911	5.766
$1h_{9/2}$	0.775	0.915	5.821

It is perhaps more interesting to compare the results for N_{nlj} of the present work with those from Refs. 14 and 28. Here our results are uniformly higher than those of Johnson *et al.*[14] by typically 0.01–0.03 for the hole states. Consequently, our occupation numbers are lower than in Ref. 14 by about the same amount for the particle states. Thus, the present model contains less depletion of the Fermi sea than Ref. 14 which, in turn, contains less depletion than the VMA results of Ref. 28. Since all three calculations appear to have somewhat less depletion than is required to describe the quenching factors derived from ^{207}Pb(e,e') experiments,[29] the present results seem to be going in the wrong direction.

One further comparison can be made. Mahaux and Ngô[27] have suggested that little difference is expected in the occupation of single-proton and single-neutron states close to the Fermi energy. Hence, Johnson *et al.*[14] cite the close agreement between their model value of $N^{(n)}_{3p_{1/2}}=0.86$ and the experimental result $N^{(p)}_{3s_{1/2}}=0.82\pm0.09$ obtained from $(e,e'p)$ reactions on ^{205}Tl and ^{206}Pb (Ref. 30) and from elastic electron scattering from ^{205}Tl and ^{206}Pb (Ref. 31). Since our value of $N^{(n)}_{3p_{1/2}}=0.90$ is larger than that in Ref. 14, the comparison seems again to be unfavorable to the present work. Recently, however, Grabmayr *et al.*[32] have reanalyzed the proton shell closure of ^{208}Pb by studying ratios of spectroscopic factors in proton pickup reactions on ^{205}Tl, ^{206}Pb, and ^{208}Pb. They invoke a sum rule in order to minimize the influence of reaction mechanisms and obtain $N^{(p)}_{3s_{1/2}}=0.92\pm0.19$ which is even larger than our own result. Their final value for this occupation number, based on a weighted average of particle transfer and $(e,e'p)$ results, is 0.88 ± 0.15. Even though all of these results are consistent within the substantial errors in the experimental values, the new results do suggest a smaller depletion of the valence shells by short-range and tensor correlations than has been commonly discussed in recent years.

Model calculations for the rms radius for each single-particle state are given for completeness in Table V. The result show the same general trends as those in Refs. 14 and 28, but the present radii are somewhat smaller. Whether these differences are significant is not clear but may provide an interesting comparison for some future program of $(e,e'n)$ studies.

VII. DISCUSSION

Lawson, Guenther, and Smith[8] recently reported a detailed analysis of neutron scattering from ^{209}Bi from 1.5 to 10.0 MeV which included conventional energy-

dependent optical-model analysis plus consideration of the effects of the dispersion correction [Eqs. (1) and (2)] at low energy. Their work included new measurements of neutron scattering ranging from 4.5 to 10.0 MeV plus older works[9,10] between 1.5 and 4 MeV. Their analysis also included an evaluation of neutron total cross sections from 0.5 to 20 MeV. The present analysis retains the 1.5- to 4.0-MeV data of Refs. 9 and 10 and includes our previous differential cross-section data from 4.0 to 7.0 MeV,[5] presents unpublished independent scattering measurements at 7.5, 8.0, 9.0, and 10.0 MeV and new scattering data at 11.0, 12.0, 20.0, and 24.0 MeV and new total cross-section measurements from ORELA from 0.83 to 60 MeV. The recent scattering data by Olsson *et al.*[16] at 21.6 MeV are also included in the analysis. In the region of overlap, the new scattering data are in excellent agreement with the 4.5- to 10.0-MeV data of Ref. 8. Moreover, the corrections for compound elastic scattering in Ref. 8 are essentially the same as those used in Ref. 5 and the present work. The point to emphasize here is that the energy range of the present work is considerably expanded over that of Ref. 8. The narrow energy range of the LGS analysis resulted in several difficulties that are removed in the new analysis: (1) The dispersion integral in Ref. 8 included only a Woods-Saxon derivative or surface absorption term. While this restriction is adequate for a phenomenological description of the scattering for $E_n < 10$ MeV, the dispersion integral extends from $-\infty$ to $+\infty$. Thus, the dispersion correction ΔV in Ref. 8 contains ΔV_S but not ΔV_V. The present work removes this shortcoming by developing a complete model for W_S and W_V at all energies. Indeed, our model for W_V would benefit from more data at higher energies. This is why we measured σ_T up to 60 MeV. (2) Much emphasis is placed in Ref. 8 on locating the energy at which $dJ_V(E)/dE$ changes sign with the conclusion that the only maximum in $J_V(E)$ occurs at $E < 0$. In the present work (Fig. 7), the predicted maximum occurs close to $+2$ MeV in fair agreement with the values obtained in Refs. 14 and 28. Nevertheless, we agree with the general observation of LGS that the Fermi surface anomaly is only striking when bound-state data are considered together with the scattering data. (3) LGS conclude that the slope of $J_V(E)$ vs E changes in the vicinity of 10 MeV. This result is also obtained in the present work. See Fig. 7 again for the model predictions for $J_V(E)$ over the entire energy range -20 to $+40$ MeV.

It remains to compare the results of the present work with the Johnson, Horen, and Mahaux study of ^{208}Pb (Ref. 14). The spirit of the present analysis was largely guided by that pioneering development of the DOMA. The similarities are very great considering the fact that the positive-energy inputs to the model had no data in common. Specifically, we obtain practically the same values for the geometrical parameters r_H, a_H, r_S, and a_S and derive a very similar expression [Eq. (12)] for the Hartree-Fock-type potential. The principal difference between the analyses concerned the functional forms for $W_S(E)$ and $W_V(E)$. Linear segments were used in Ref. 14 while the more realistic forms given in Eq. (9) were used in the present work. Our motivation for this choice had to do with the limited success of Ref. 14 in describing the scattering data and σ_T below 10 MeV in their original form of the DOMA. We experienced the same difficulties when we applied the linear segment (LS) model to the ^{209}Bi data.[19] The difficulty is presumably due to the discontinuous change in the slope of W_S in this neighborhood. Detailed comparisons of the scattering from ^{209}Bi were made with each prescription for the functional forms of $W_S(E)$ and $W_V(E)$. Indeed the value of χ^2 per point was at least a factor of 2 worse with the LS model between 4.5 and 9 MeV and slightly worse at higher energies. Conversely, the LS model was slightly better between 2 and 3 MeV, but, at this very low energy, compound elastic scattering makes up about $\frac{1}{3}$ of the total cross section so the sensitivity of the final data for shape elastic scattering to the Hauser-Feshbach calculations for compound elastic scattering is much greater here than at higher energies. Finally, the χ^2 per point for the total cross-section data was 27% better with the present model than with the LS model. We conclude that the present model for $W_S(E)$ and $W_V(E)$ is distinctly superior to the LS model for neutron scattering from ^{209}Bi.

The minor and straightforward improvement in the DOMA given by Eqs. (9) and (10) would not normally be given such emphasis. In the case of $n + ^{208}$Pb, however, the deficiencies of the original DOMA of Ref. 14 in the low-energy domain have given rise to several explanations[14,33,34] involving new physics ideas such as angular-momentum-dependent absorption and energy-dependent imaginary potential geometry. While some of these ideas might indeed be important, it might be better to defer those explanations until after the rough features of the original model [i.e., discontinuous derivatives for both $W_S(E)$ and $W_V(E)$] have been replaced with more realistic representations. We emphasize again that the improvement obtained with Eq. (9) has been demonstrated only for ^{209}Bi and only for positive energies.

VIII. CONCLUSIONS

New measurements of differential elastic neutron scattering from ^{209}Bi above 10 MeV and total cross setup up to 60 MeV have been presented. These data, together with earlier measurements from several laboratories, provide a very extensive data base for this target nucleus and thus provide a rich resource with which to study the finer details of the optical-model potential. The central focus of the present work was the application of the dispersive optical-model analysis to ^{209}Bi. The application was successful in that the resulting Hartree-Fock-type term was smoothly varying over a wide energy region. Moreover, the "anomalous" features of the scattering potential (e.g., energy-dependent geometry at low energies) were well described by a dispersion correction.

The dispersion correction provides a straightforward, parameter-free recipe to extrapolate the well-determined optical potential at positive energy into the shell-model domain at negative energy. In order to test the success of this extrapolation, we made the unusual but highly plau-

sible assumption that the single neutron states in ^{209}Bi were the same as the single neutron states in ^{208}Pb. With this assumption we obtained single-particle energies, spectroscopic factors, and occupation numbers for the single-particle states. These "lead-derived-from-bismuth" shell-model properties were very similar to the "lead-derived-from-lead" properties obtained by Johnson, Horen, and Mahaux[14] thus justifying the assumption mentioned above and verifying the somewhat larger energy extrapolation required in Ref. 14. Small systematic differences were noted in the occupation probabilities for single neutron states obtained from these two approaches to the ^{208}Pb shell-model potential. It is tempting to claim that the present values are preferred set since the present model has some advantages in describing the scattering data below 10 MeV. Some support for this viewpoint comes from the recent work by Grabmayr *et al.*[32] who find less depletion of the Fermi sea from their study of particle transfer reactions than they had reported earlier from $(e,e'p)$ measurements. However, two words of caution are required before this claim should be taken too seriously. (1) The uncertainties in the experimental values for the occupation probabilities are still larger than the differences between Ref. 14 and the present work. (2) Some problems remain in the extraction of absolute spectroscopic factors and occupation probabilities obtained via dispersion corrections. The most serious problem has to do with the assumption that the imaginary potential $W(r,E')$ is symmetric about $E'=E_F$ even for larger values of $|E'|$. A more realistic model for $W(r,E')$ at large $|E'|$ would have little influence on the description of the scattering data at moderate energy or even on the calculated energies of the single particle states. Mahaux and co-workers[27,28] have cautioned, however, that the division of the full potential in $V_H(r,E)$ and $\Delta V(r,E)$, and, thus, the occupation probabilities and spectroscopic factors, would be sensitive to the asymptotic behaviors of $W(r,E')$. This problem is certainly worthy of further attention.

ACKNOWLEDGMENTS

The authors wish to acknowledge the assistance of J. Petler, D. Wang, and Y. Wang during the measurements of the differential cross sections. The technical expertise of Dave Sturbois and Don Carter proved invaluable in the running of the experiments. Very special thanks go to Jack A. Harvey for his hospitality and guidance during the measurement of total cross sections at ORELA. This work was supported by the National Science Foundation under Grant Nos. PHY-8507137 and 8810220.

*Present address: Triangle Universities Nuclear Laboratory, Durham, NC 27706.

[1]R. W. Finlay, J. R. M. Annand, T. S. Cheema, J. Rapaport, and F. S. Dietrich, Phys. Rev. C **30**, 796 (1984).

[2]R. W. Finlay, J. R. M. Annand, J. S. Petler, and F. S. Dietrich, in *Neutron-Nucleus Collisions—A Probe at Nuclear Structure (Burr Oak State Park, Glouster, Ohio),* Proceedings of the Conference on Neutron-Nucleus Collisions—A Probe of Nuclear Structure, AIP Conf. Proc. **124**, edited by J. Rapaport, R. W. Finlay, S. M. Grimes, and F. S. Dietrich (AIP, New York, 1984).

[3]R. W. Finlay, J. R. M. Annand, J. S. Petler, and F. S. Dietrich, Phys. Lett. B **155**, 313 (1985); **157**, 475 (1985).

[4]C. Mahaux and H. Ngô, Nucl. Phys. **A378**, 205 (1982).

[5]J. R. M. Annand, R. W. Finlay, and F. S. Dietrich, Nucl. Phys. **A443**, 249 (1985).

[6]C. Mahaux and R. Sartor, Nucl. Phys. **A460**, 466 (1986).

[7]R. W. Finlay, J. Wierzbicki, R. K. Das, and F. S. Dietrich, Phys. Rev. C **39**, 804 (1986).

[8]R. D. Lawson, P. T. Guenther, and A. B. Smith, Phys. Rev. C **36**, 1298 (1987).

[9]A. Smith, P. Guenther, and J. Whalen, Nucl. Sci. Eng. **75**, 69 (1980).

[10]N. Olsson, B. Holmqvist, and E. Ramström, Nucl. Phys. **A385**, 285 (1983).

[11]R. L. Walter and P. P. Guss, in *Nuclear Data in Basic and Applied Sciences,* edited by P. G. Young, R. E. Brown, G. F. Auchampaugh, P. W. Lisowski, and L. Stewart (Gordon and Breach, New York, 1986), Vol. 2, p. 1079.

[12]C. Mahaux and R. Sartor, Nucl. Phys. **A468**, 193 (1987), and references therein.

[13]J. P. Delaroche, Y. Wang, and J. Rapaport, Phys. Rev. C **39**, 391 (1989).

[14]C. H. Johnson, D. J. Horen, and C. Mahaux, Phys. Rev. C **36**, 2252 (1987).

[15]C. Mahaux and R. Sartor, Nucl. Phys. **A484**, 205 (1988).

[16]R. W. Finlay and J. S. Petler, in *Proceedings of the Use of the Optical Model for the Calculation of Neutron Cross Sections Below 20 MeV, Paris, France, 1986* (Organization for Economic Cooperation and Development–Nuclear Energy Agency, Paris, 1986).

[17]D. C. Larson, J. A. Harvey, and N. W. Hill, in *Nuclear Cross Sections for Technology,* Natl. Bur. Stand. (U.S.) Spec. Pub. No. 594, edited by J. L. Fowler, C. H. Johnson, and C. D. Bowman (U.S. GPO, Washington, D.C., 1979).

[18]N. Olsson, B. Trostell, E. Ramström, B. Holmqvist, and F. S. Dietrich, Nucl. Phys. **A472**, 237 (1987).

[19]F. G. Perey, computer code GENOA, private communication, 1975.

[20]J. R. M. Annand, computer code OPSTAT, private communication, 1988.

[21]R. K. Das, R. W. Finlay, and J. A. Harvey, Bull. Am. Phys. Soc. **33**, 964 (1988).

[22]F. G. Perey and B. Buck, Nucl. Phys. **32**, 353 (1962).

[23]J. Rapaport, Phys. Rep. **87**, 25 (1982).

[24]M. R. Schmorak, Nucl. Data Sheets **22**, 487 (1977).

[25]M. J. Martin, Nucl. Data Sheets **22**, 545 (1977).

[26]S. Galès, Nucleonik **27**, 82 (1982).

[27]C. Mahaux and H. Ngô Nucl. Phys. **A431**, 486 (1984).

[28]C. Mahaux and R. Sartor, Nucl. Phys. **A493**, 157 (1989).

[29]C. Papanicolas, in *Nuclear Structure at High Spin, Excitation and Momentum Transfer (McCormick's Creek State Park, Bloomington, Indiana),* Proceedings of the Workshop on Nuclear Structure at High Spin, Excitation and Momentum

Transfer, AIP Conf. Proc. No. 142, edited by H. Nann (AIP, New York, 1985).
[30]E. N. M. Quint *et al.*, Phys. Rev. Lett. **58**, 1088 (1987).
[31]J. M. Cavedon *et al.*, Phys. Rev. Lett. **49**, 978 (1982); B. Frois *et al.*, Nucl. Phys. **A396**, 409c (1983).
[32]P. Grabmayr, G. J. Wagner, H. Clement, and H. Röhm, Nucl. Phys. **A394**, 244 (1989).
[33]C. H. Johnson and R. R. Winters, Phys. Rev. C **37**, 2340 (1988).
[34]J. P. Jeukenne, C. H. Johnson, and C. Mahaux, Phys. Rev. C **38**, 2573 (1988).